

Approximate Amplitude Encoding with the Adaptive Interpolating Quantum Transform

Gekko Budiutama^{1,2*}, Shunsuke Daimon^{3*}, Xinchu Huang^{1,2}, Hirofumi Nishi^{1,2},
Yu-ichiro Matsushita^{1,2,3}

¹Quemix Inc., Taiyo Life Nihonbashi Building, 2-11-2 Nihonbashi, Chuo-ku, Tokyo, 103-0027, Japan.

²Department of Physics, The University of Tokyo, Tokyo, 113-0033, Japan.

³Quantum Materials and Applications Research Center, National Institutes for Quantum Science and Technology (QST), Tokyo, 152-8550, Japan.

*E-mails: bgekko@quemix.com; daimon.shunsuke@qst.go.jp;

Abstract

Amplitude encoding of real-world data on quantum computers is often the workflow bottleneck: direct amplitude encoding scales poorly with input size and can offset any speedups in subsequent processing. Fourier-based sparse amplitude encoding lowers cost by retaining only a small subset of dominant coefficients, but its fixed, non-adaptive basis leads to significant information loss. In this work, we replace the Fourier transform with the adaptive interpolating quantum transform (AIQT) in the sparse amplitude encoding workflow. The AIQT learns a data-adapted basis that concentrates information into a small number of coefficients. Consequently, at matched sparsity, the AIQT retains more information and achieves lower reconstruction error compared to the Fourier baseline. On financial time-series data, the AIQT reduces reconstruction error by 40% relative to the Fourier baseline, and on image datasets the reduction is up to 50% at the same sparsity level, with nearly identical encoding gate cost. Crucially, the approach preserves the efficiency of Fourier-based methods: the AIQT is built on the structure of the quantum Fourier transform circuit. Its gate count scales quadratically with the number of qubits, while classical evaluation can be carried out in quasilinear time. In addition, the AIQT is trained without labels and does not require sampling from quantum hardware or a simulator, removing a major bottleneck in data-driven amplitude-encoding methods.

Quantum computing has made steady progress toward practical applications in areas such as quantum chemistry, optimization, and quantum machine learning¹⁻⁹. In these applications, encoding classical data onto a quantum device is a prerequisite for any end-to-end advantage.

Amplitude encoding is a widely used method that maps a length- N vector to the amplitudes of the computational-basis states of an n -qubit system ($n = \log_2 N$). Generic amplitude encoding methods require either an exponential number of two-qubit gates

or an exponential number of ancilla qubits, which can cancel out any downstream speedup¹⁰⁻¹⁵. Under certain data assumptions, polynomial-time methods exist, for example for structured probability distributions or localized basis expansions, but their practical effectiveness is often curtailed by device noise and calibration limitations¹⁶⁻²⁰. NISQ-friendly amplitude-encoding circuits based on data-driven quantum circuit models have also been proposed²¹⁻²⁴, but they typically rely on explicit quantum circuit evaluation

on hardware or high-fidelity simulators, either during variational training or for large-scale circuit synthesis.

One practical way to lower the cost of amplitude encoding is to prepare an approximate state by extracting dominant coefficients²⁵⁻²⁷. In this workflow, a classical transform (e.g., Fourier or Walsh-Haar) is applied to the input to obtain its coefficients in the transform basis. The dominant coefficients are then selected and the rest discarded. Amplitude encoding is applied to the retained coefficients, and the original vector is approximately reconstructed via the inverse transform. However, this sparse encoding workflow is inherently lossy: the use of a fixed transform across datasets can drop non-dominant yet task-relevant details. For example, edges, textures, and transients are not compactly represented in a Fourier basis, which can raise reconstruction error for images or non-smooth time series. While methods to improve the expressiveness of fixed transforms exist²⁸, it is not clear how to translate these learned transforms into compact, hardware-efficient quantum circuits.

To address this limitation, we apply the Adaptive interpolating quantum transform (AIQT) to sparse amplitude encoding. Introduced in our prior work²⁹, the AIQT is a quantum-native, unitary, compactly parameterized transform that adapts its basis to the data. The AIQT is trained to maximize the information captured by the retained coefficients, reducing information loss in the sparse selection step. Empirically, at matched sparsity, the AIQT outperforms Fourier baselines, reducing reconstruction error by 40% on 1D signals and up to 50% on 2D images. Unlike prior data-driven amplitude-encoding methods, our training pipeline operates entirely on classical data and does not require sampling from a quantum device or simulator at any stage. Moreover, since the AIQT is built on the efficient circuit structure of the quantum Fourier transform, its gate count scales polynomially (quadratically) with the number of qubits.

Transform-based Approximate Amplitude Encoding

The general workflow for transform-based approximate amplitude encoding proceeds as follows. For an input $\mathbf{x} \in \mathbb{R}^N$, a unitary transform U is first applied on a classical computer to obtain complex coefficients $\mathbf{y}(\mathbf{x}) = U\mathbf{x} \in \mathbb{C}^N$. Let $\mathcal{K}(\mathbf{x})$ index the k coefficients of $\mathbf{y}(\mathbf{x})$ with largest squared magnitude. The corresponding sparse coefficient vector $\tilde{\mathbf{y}}(\mathbf{x}) \in \mathbb{C}^N$ is

defined by

$$\tilde{y}_j(\mathbf{x}) = \begin{cases} y_j(\mathbf{x}), & j \in \mathcal{K}(\mathbf{x}), \\ 0, & j \notin \mathcal{K}(\mathbf{x}). \end{cases} \quad (1)$$

The normalized truncated coefficient is then defined as

$$\phi_j(\mathbf{x}) = \frac{\tilde{y}_j(\mathbf{x})}{\left(\sum_{\ell=1}^N |\tilde{y}_\ell(\mathbf{x})|^2\right)^{1/2}}. \quad (2)$$

On the quantum device, a sparse state-preparation circuit encodes these coefficients into an $n = \log_2 N$ qubit state,

$$|\phi(\mathbf{x})\rangle = \sum_{j=1}^N \phi_j(\mathbf{x}) |j\rangle. \quad (3)$$

Finally, an inverse transform U^{-1} is implemented as a quantum circuit, yielding an approximate reconstruction of the original vector,

$$|\tilde{\psi}(\mathbf{x})\rangle = U^{-1}|\phi(\mathbf{x})\rangle. \quad (4)$$

Here, $|\tilde{\psi}(\mathbf{x})\rangle$ denotes the reconstructed state that approximates the exact amplitude-encoded state $|\psi(\mathbf{x})\rangle$, where $|\psi(\mathbf{x})\rangle = \frac{1}{\|\mathbf{x}\|_2} \sum_{j=1}^N x_j |j\rangle$.

Several approximate state-preparation methods fit into this workflow. The first proposal uses the Fourier transform and refers to this scheme as the Fourier series loader (FSL)²⁵. More recent work instantiates the same hybrid template with the Walsh-Haar transform in place of the Fourier transform, improving the scaling of the inverse transform while otherwise following the same overall workflow²⁷. In this work we consider the Fourier-based instance, the FSL, to be our baseline transform-based approximate amplitude-encoding scheme.

From a resource point of view, the FSL workflow consists of a classical preprocessing step to compute $\mathbf{y}(\mathbf{x})$ and select the top- k coefficients, followed by sparse amplitude encoding and an inverse transform on the quantum device. Among sparse state-preparation methods, the worst-case circuit size scales as $O\left(\frac{nk}{\log n} + n\right)$ ³⁰⁻³⁶. Thus, the end-to-end cost for the FSL is $O(N \log N)$ on the classical side for preprocessing (dominated by the FFT) and $O\left(\frac{nk}{\log n} + n + n^2\right)$ on the quantum side for sparse amplitude encoding followed by the inverse transform. In regimes

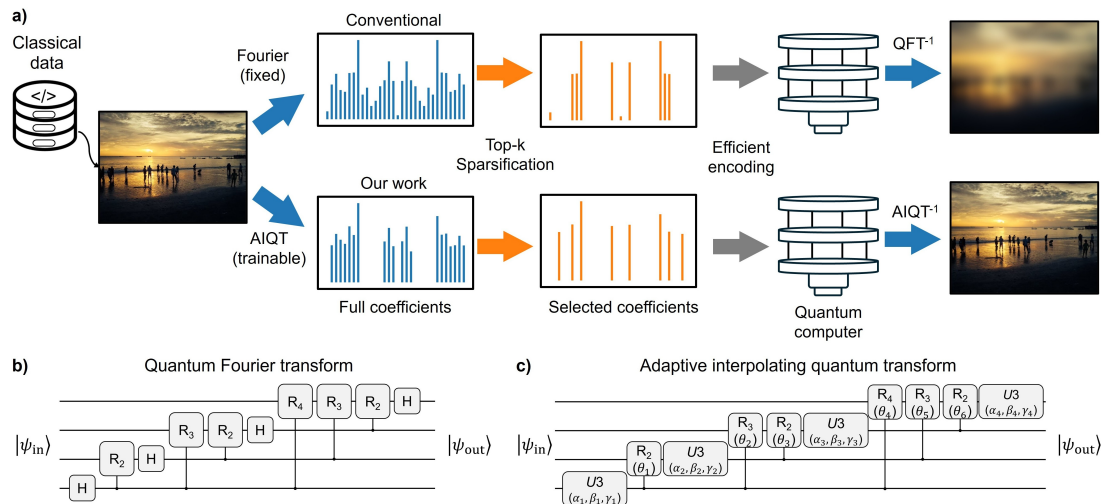


Fig. 1 Sparse amplitude encoding workflows with Fourier (FSL) and AIQT transforms and their quantum circuits. a) Sparse amplitude encoding with the Fourier State Loader (FSL). A Fourier transform is first applied to the classical data \mathbf{x} , producing the full set of coefficients \mathbf{y} . We then keep the k largest-magnitude coefficients and set the rest to zero, yielding a k -sparse vector $\tilde{\mathbf{y}}$. This vector is amplitude encoded on the quantum computer to obtain the state $|\tilde{\phi}\rangle$. Finally, an approximate reconstruction of the data is obtained by applying the inverse quantum Fourier transform, producing the state $|\tilde{\psi}\rangle_{\text{FSL}}$. Here, the first and middle Fourier coefficients are always included, regardless of k , to maintain symmetry. Thus, for a given k , the FSL selects the top- k coefficients with 2 additional coefficients. b) The proposed sparse amplitude encoding uses the Adaptive interpolating quantum transform (AIQT) and its inverse in place of the Fourier transform. The AIQT is trained to maximize the amount of information preserved during coefficient truncation, which leads to lower reconstruction error. Moreover, the AIQT does not enforce conjugate symmetry, thus we simply select the top- k coefficients without any additional symmetry-preserving sampling. c) The Quantum Fourier Transform (QFT) circuit used in FSL. d) The AIQT circuit is constructed by parameterizing the QFT structure with single-qubit gates $U3(\alpha, \beta, \gamma)$ and controlled-phase gates $CR(\theta)$, yielding $U_{\text{AIQT}}(\theta, \alpha, \beta, \gamma)$. Here, $U3(\alpha, \beta, \gamma) = \begin{bmatrix} \cos(\alpha/2) & -e^{i\gamma} \sin(\alpha/2) \\ e^{i\beta} \sin(\alpha/2) & e^{i(\beta+\gamma)} \cos(\alpha/2) \end{bmatrix}$ and $CR(\theta) = \text{diag}(1, 1, 1, e^{i\theta})$.

where the target states admit good k -sparse approximations with $k \ll N$, this method uses fewer quantum gates than generic amplitude-encoding schemes, whose worst-case circuit size scales linearly in N for arbitrary states.

The Adaptive Interpolating Quantum Transform for Amplitude Encoding

The adaptive interpolating quantum transform (AIQT) is a framework for constructing trainable unitary transforms that interpolate among a set of predefined quantum transforms. In general, the AIQT framework is circuit agnostic: it can be instantiated using different efficient quantum circuits, with interpolation achieved by embedding trainable parameters into them²⁹.

For this work, we utilized a parametrized variant of the quantum Fourier transform (Figs. 1b and c). Specifically, we replace each Hadamard and single-qubit phase gate by a generic single-qubit gate $U3(\alpha, \beta, \gamma) = \begin{bmatrix} \cos(\alpha/2) & -e^{i\gamma} \sin(\alpha/2) \\ e^{i\beta} \sin(\alpha/2) & e^{i(\beta+\gamma)} \cos(\alpha/2) \end{bmatrix}$, and parametrize the controlled phase gates as $CR(\theta) = \text{diag}(1, 1, 1, e^{i\theta})$. With this parameterization, the

AIQT smoothly interpolates between the quantum Fourier transform, the Hadamard transform, and the identity as its parameters vary. We choose this AIQT for two reasons: (i) like the FFT, this AIQT admits a butterfly-style factorization, yielding an $O(N \log N)$ classical algorithm; and (ii) the corresponding quantum implementation on $n = \log_2 N$ qubits has a gate count of $O(n^2)$.

Figure 1a shows that the AIQT-based approximate amplitude-encoding workflow follows the same transform-based pipeline as the FSL baseline. For a real input $\mathbf{x} \in \mathbb{R}^N$, applying the AIQT unitary $U_{\text{AIQT}}(\theta, \alpha, \beta, \gamma)$ yields complex transform coefficients $\mathbf{y}(\mathbf{x}) = U_{\text{AIQT}} \mathbf{x}$. The sparse coefficient vector $\tilde{\mathbf{y}}(\mathbf{x})$ is obtained by retaining only those entries whose indices are in $\mathcal{K}(\mathbf{x})$, where $\mathcal{K}(\mathbf{x})$ denotes the index set of the k largest squared-magnitude coefficients of $\mathbf{y}(\mathbf{x})$, and setting all remaining entries to zero. This sparse vector is amplitude encoded on the quantum computer to obtain $|\phi(\mathbf{x})\rangle$, and an approximate reconstruction of \mathbf{x} is recovered by applying the inverse transform U_{AIQT}^{-1} .

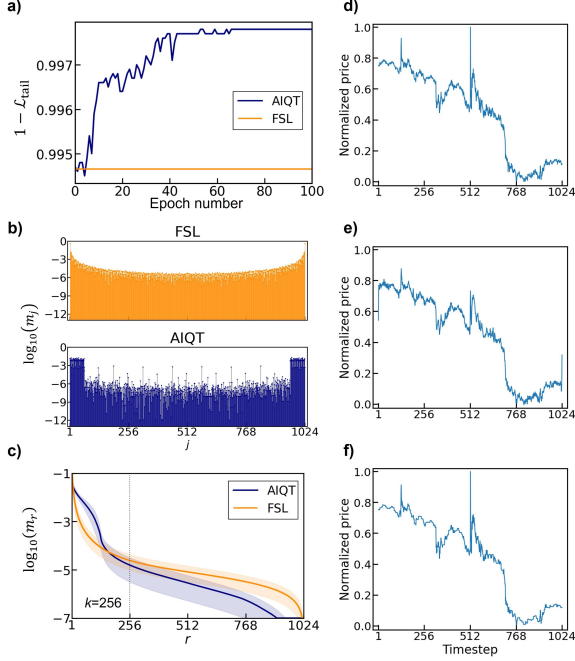


Fig. 2 Coefficient statistics and single-sample reconstructions for the AIQT and the FSL. a) Squared magnitude of the top-256 coefficients as a function of training epoch for the AIQT (blue), compared with the fixed FSL baseline (orange). b) Distribution of squared magnitudes (m_j) across coefficient index $j \in \{1, \dots, 1024\}$ for a representative sample for FSL (top, orange) and AIQT (bottom, blue). c) Average squared magnitude (m_r) as a function of rank r for the AIQT (blue) and the FSL (orange). For each input, coefficients are sorted in descending order from largest (m_1) to smallest (m_{1024}), and we then average m_r over the dataset. Solid lines show the dataset mean, and shaded regions indicate standard deviation.

d-f) Single-sample visualization showing the original signal (d), the FSL reconstruction (e), and the AIQT reconstruction (f), all at matched sparsity ($k = 256$).

To train the AIQT, we first define the normalized squared magnitudes

$$m_j(\mathbf{x}) = \frac{|y_j(\mathbf{x})|^2}{\sum_{\ell=1}^N |y_\ell(\mathbf{x})|^2}, \quad (5)$$

so that $\sum_j m_j(\mathbf{x}) = 1$ for each input \mathbf{x} . Here, a top- k tail loss function is used to train the AIQT to encourage the transform to concentrate information in the top- k largest coefficients:

$$\mathcal{L}_{\text{tail}} = \mathbb{E}_{\mathbf{x}} \left[\sum_{j \notin \mathcal{K}(\mathbf{x})} m_j(\mathbf{x}) \right], \quad (6)$$

where $\mathbb{E}_{\mathbf{x}}[\cdot]$ denotes the average over the dataset.

Table 1 Performance of the FSL vs the AIQT across sparsity k on the one-dimensional finance dataset.

k	Method	Train		Validation	
		cRMSE $\times 10^{-3}$	F	cRMSE $\times 10^{-3}$	F
64	AIQT	4.144	0.9826	4.197	0.9821
	FSL	—	—	4.659	0.9780
128	AIQT	2.462	0.9938	2.468	0.9938
	FSL	—	—	3.308	0.9888
256	AIQT	1.471	0.9978	1.455	0.9978
	FSL	—	—	2.283	0.9947
384	AIQT	1.055	0.9989	1.036	0.9989
	FSL	—	—	1.731	0.9969

We evaluate both AIQT and the FSL baseline by comparing their reconstructed states $|\tilde{\psi}_{\text{AIQT}}(\mathbf{x})\rangle$ and $|\tilde{\psi}_{\text{FSL}}(\mathbf{x})\rangle$ to the exact amplitude-encoded state $|\psi(\mathbf{x})\rangle$, using the complex root-mean-squared error (cRMSE) and the fidelity F (see Methods).

Results

The AIQT for efficient amplitude encoding

Figure 2a shows the total squared magnitude captured by the top- k coefficients ($1 - \mathcal{L}_{\text{tail}}$) with $k = 256$ (25% of $N = 1024$). The AIQT (blue) quickly surpasses the FSL (orange, $1 - \mathcal{L}_{\text{tail}} \approx 0.995$) and converges to a higher plateau ($1 - \mathcal{L}_{\text{tail}} \approx 0.998$), indicating that the AIQT basis consistently concentrates more information into the top-256 set than Fourier.

Figure 2b shows a representative example of how the squared-magnitude coefficients m_j are distributed across index j for the FSL (top, orange) and the AIQT (bottom, blue). In this example, the FSL spreads the squared magnitudes m_j over many Fourier modes, with an almost uniform background level except for the two dominant coefficients at $j = 2$ and its conjugate-symmetric pair at $j = 1024$. In contrast, the AIQT (bottom, blue) concentrates more information into the first and last ~ 50 bins and into a small number of pronounced coefficients in the middle of the spectrum, while pushing the remaining coefficients down to a much lower background level. This visualization shows how the AIQT reshapes the input so that as much information as possible is concentrated into the top- k coefficients, reducing the loss incurred during the truncation step.

Figure 2c shows the dataset-averaged squared magnitude m_r as a function of rank r , where coefficients are ranked in descending order of squared magnitude for each input, with $r = 1$ corresponding to the largest coefficient and $r = 1024$ to the smallest. The vertical black dotted line marks $r = k$. Compared to the FSL (orange), the AIQT (blue) concentrates more information to the leading ranks and less to the tail: the blue curve lies above the orange curve for $r \leq k$ and below for $r > k$, indicating a steeper decay beyond the kept coefficients. Shaded bands show across-sample variability and confirm that this shift of coefficient magnitude toward the top- k coefficients is systematic rather than due to a few outliers.

Figures 2d–f show a single-sample comparison: (d) the original time series, (e) the FSL reconstruction using the top-256 Fourier coefficients, and (f) the AIQT reconstruction using the top-256 AIQT coefficients. Under the same 256-coefficient budget, both reconstructions follow the overall trend, but the AIQT result better preserves turning points and local variations. For instance, the AIQT recovers a prominent peak that is noticeably smoothed out in the FSL reconstruction. This qualitative behavior is consistent with the higher information capture in Fig. 2a and the steeper rank profile in Fig. 2c.

Table 1 compares the FSL and the AIQT across sparsity levels k on the one-dimensional finance dataset. The FSL is a fixed (non-trainable) Fourier transform, so its entries are reported only on the validation split, whereas the AIQT is trained on the training split and evaluated on both splits. Across all k , the AIQT achieves lower cRMSE and higher fidelity than that of the FSL. The improvement grows with sparsity: at $k = 64$, the AIQT reduces validation cRMSE from 4.659×10^{-3} to 4.197×10^{-3} , a reduction of roughly 10%, while at $k = 384$ the validation cRMSE drops from 1.731×10^{-3} to 1.036×10^{-3} , about a 40% reduction, with fidelity increasing from 0.9969 to 0.9989.

Figure 3 shows the relationship between reconstruction error (cRMSE) and the number of retained coefficients (k) for the FSL (orange) and the AIQT (blue). As discussed, k directly determines the cost of sparse amplitude encoding on a quantum computer: preparing a k -sparse state has worst-case circuit size scaling as $O(\frac{nk}{\log n} + n)$ ^{30–36}. Compared to the FSL, the error decays more rapidly with k for the AIQT, with $\text{cRMSE} \propto k^{-0.772}$ rather than that of the FSL ($\text{cRMSE} \propto k^{-0.546}$). Thus, on the finance dataset,

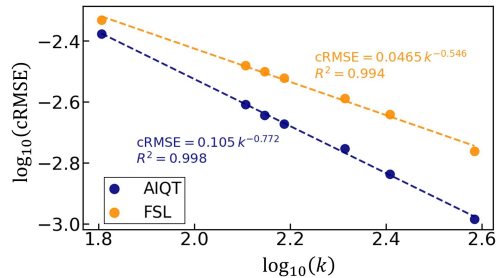


Fig. 3 Reconstruction error (cRMSE) as a function of retained coefficients (k) for the FSL and the AIQT on the finance dataset. Dashed lines denote power-law fits ($\text{cRMSE} = Ak^B$) obtained by ordinary least squares on log-transformed data. The coefficient of determination (R^2) denotes the goodness of fit for the linearized model in log space.

the AIQT does not merely improve upon the FSL by a constant factor, but instead improves the scaling of the workflow, becoming increasingly advantageous as higher reconstruction accuracy (higher k) is required.

Imaginary residuals in the AIQT reconstructions

As our goal is to encode real datasets as amplitudes on a quantum computer, we must be careful about any imaginary components that might arise in either the FSL or AIQT pipeline.

For the FSL, the Fourier spectrum of a real-valued input is conjugate-symmetric; therefore, as long as the truncation preserves this symmetry, the reconstructed state is purely real. In contrast, the AIQT operates in the complex domain and does not enforce this conjugate-symmetry structure, so reconstructed states can, in principle, have non-zero imaginary components even when the input is real. To quantify this imaginary leakage in the reconstruction, we define the per-sample imaginary-part norm

$$I(\mathbf{x}) = \|\text{Im}(\tilde{\psi}(\mathbf{x}))\|_2 = \left(\sum_{j=1}^N (\text{Im}(\tilde{\psi}_j(\mathbf{x})))^2 \right)^{1/2}. \quad (7)$$

We then consider its dataset average

$$\bar{I} = \mathbb{E}_{\mathbf{x}}[I(\mathbf{x})]. \quad (8)$$

For comparison, we also track the real part of the reconstruction. We define the per-sample real-part

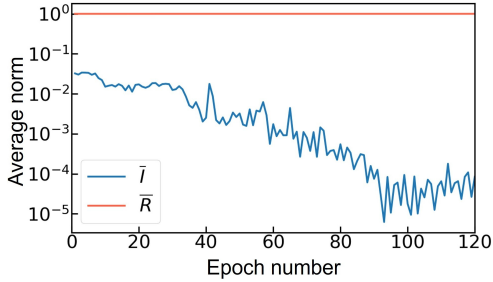


Fig. 4 Dataset-averaged imaginary-part norm \bar{I} (blue) and dataset-averaged real-part norm \bar{R} (red) of the AIQT reconstructed signal as a function of training epoch for the AIQT model with $k = 256$. The model automatically reduces leakage into the imaginary part over training.

norm

$$R(\mathbf{x}) = \left\| \text{Re}(\tilde{\psi}(\mathbf{x})) \right\|_2 = \left(\sum_{j=1}^N (\text{Re}(\tilde{\psi}_j(\mathbf{x})))^2 \right)^{1/2}, \quad (9)$$

and its dataset average

$$\bar{R} = \mathbb{E}_{\mathbf{x}}[R(\mathbf{x})]. \quad (10)$$

Figure 4 shows the evolution of the dataset-averaged norms \bar{I} (blue) and \bar{R} (red) of the reconstructed state for $k = 256$ on a logarithmic scale. Over training, \bar{I} drops by roughly three orders of magnitude, from about 10^{-2} to 10^{-5} , while \bar{R} remains essentially pinned at 1. This indicates that the AIQT learns parameters that keep almost all of the amplitude norm in the real part and drive the imaginary leakage to a negligible level.

Table 2 complements this plot by reporting the average real- and imaginary-part norms across sparsity levels k on the finance dataset. For each k we list $1 - \bar{R}$, which measures how far the average real-part norm \bar{R} deviates from 1, together with the imaginary-part norm \bar{I} , for both train and validation splits. Except at the lowest sparsity ($k = 64$), the deviation $1 - \bar{R}$ is on the order of 10^{-9} and \bar{I} is on the order of 10^{-4} to 10^{-5} , indicating that the reconstructed states are almost perfectly real-valued and that imaginary leakage remains negligible in practice. The close agreement between train and validation values further suggests that this behavior is stable and not an artifact of overfitting.

Thus, while the AIQT lacks the theoretical real-valued guarantee of the FSL, the trained models effectively recover real outputs in practice, so imaginary

Table 2 Real- and imaginary-part residual norms for the AIQT across sparsity k on the one-dimensional finance dataset.

k	Train		Validation	
	$1 - \bar{R}$	\bar{I}	$1 - \bar{R}$	\bar{I}
64	1.387×10^{-3}	4.896×10^{-2}	1.439×10^{-3}	4.975×10^{-2}
128	1.367×10^{-9}	5.204×10^{-5}	1.378×10^{-9}	5.224×10^{-5}
256	2.068×10^{-9}	6.410×10^{-5}	2.052×10^{-9}	6.385×10^{-5}
384	6.148×10^{-9}	1.106×10^{-4}	6.156×10^{-9}	1.107×10^{-4}

residuals do not pose a practical limitation for the amplitude-encoding regime considered here.

The deep AIQT architecture

So far we have focused on a single AIQT layer acting as a learned replacement for the Fourier transform. In practice, it can be beneficial to increase the expressive power of the transform by composing several such layers, in direct analogy with adding depth in a neural network.

Here we propose the deep AIQT architecture, which increases the expressive power of the transform by stacking multiple AIQT blocks.

Figure 5 depicts the deep AIQT architecture: a stack of D learnable AIQT blocks applied sequentially to the input state. Let $\boldsymbol{\eta}_d = (\boldsymbol{\theta}_d, \boldsymbol{\alpha}_d, \boldsymbol{\beta}_d, \boldsymbol{\gamma}_d)$ denote the parameters of block d . The overall unitary is

$$U_{\text{DeepAIQT}} = \prod_{d=1}^D U_{\text{AIQT}}(\boldsymbol{\eta}_d), \quad (11)$$

where the factors are ordered so that $d = 1$ acts first on the input state. This construction retains the unitarity and FFT-like structure of a single AIQT layer, but increases expressivity by composing multiple trainable transforms. Because each block has $O(N \log N)$ classical cost and $O(n^2)$ quantum gate count (with $N = 2^n$), the overall deep AIQT scales linearly in the number of layers D , providing a principled way to trade computation for representational power.

Figure 6 summarizes the training dynamics of the deep AIQT for MNIST (top row) and CIFAR-RGB (bottom row). Figures 6a and c show the total squared magnitude captured by the top- k coefficients, while Fig. 6b and d show the dataset-averaged imaginary-part norm \bar{I} on a logarithmic scale. In both datasets, all AIQT configurations outperform the FSL (orange)

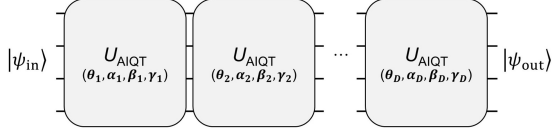


Fig. 5 The deep AIQT architecture. A depth- D stack of AIQT blocks with independent parameters applied sequentially to the input state.

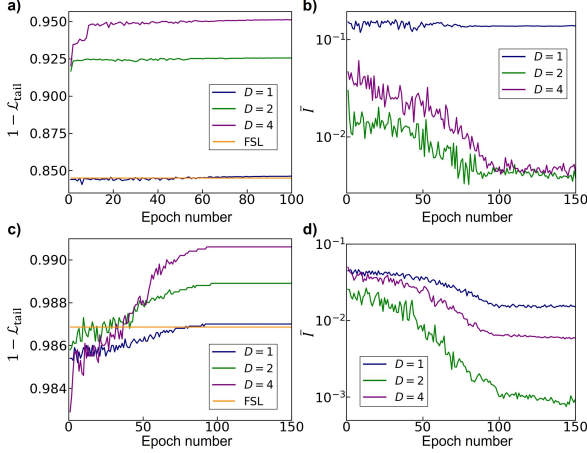


Fig. 6 Training dynamics of the deep AIQT on MNIST and CIFAR-RGB. a,b) MNIST results for depths $D \in \{1, 2, 4\}$ showing the squared magnitude of the dominant coefficients and the average imaginary-part norm $\bar{\Gamma}$. c,d) CIFAR-RGB results shown in the same format. Sparsity is fixed to $k = 52$ for MNIST and $k = 154$ for CIFAR-RGB.

in terms of the square magnitude concentration, and increasing the depth from $D = 1$ (blue) to $D = 4$ (purple) yields a significant improvement (Figs. 6a and c). For MNIST, deeper models also significantly suppress imaginary leakage: $\bar{\Gamma}$ decreases by more than an order of magnitude during training, with $D = 2$ (green) and $D = 4$ (purple) converging to much smaller values than $D = 1$ (Fig. 6b). On CIFAR-RGB, all depths reduce $\bar{\Gamma}$ relative to initialization, and the intermediate depth $D = 2$ (green) achieves the smallest imaginary residual (Fig. 6d). In all configurations, the final values of $\bar{\Gamma}$ are small enough that imaginary leakage is negligible for the approximate amplitude-encoding regime considered here.

Figure 7a compares MNIST reconstructions at matched sparsity $k = 52$ using the deep AIQT with depth $D = 4$. Relative to the FSL, the deep AIQT produces sharper digit strokes, cleaner junctions, and fewer directional artifacts, yielding images that are visually closer to the reference rows. The FSL reconstructions exhibit noticeable blurring around edges.

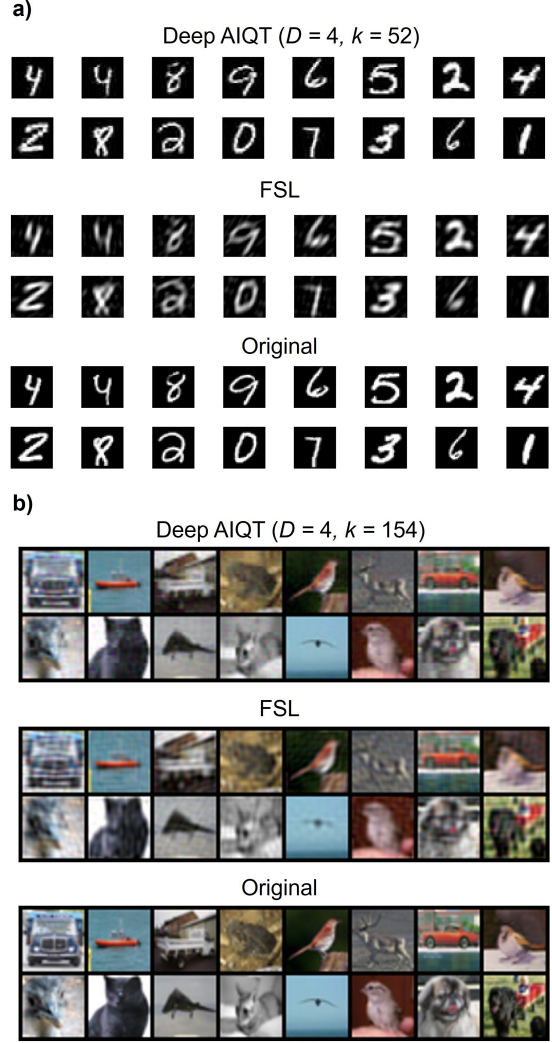


Fig. 7 Image reconstructions at matched sparsity using the deep AIQT and the FSL. a) MNIST reconstructions at $k = 52$ comparing the deep AIQT ($D = 4$) with the FSL. b) CIFAR-RGB reconstructions at $k = 154$ comparing the deep AIQT ($D = 4$) with the FSL. In each panel, the bottom row shows the original images.

Figure 7b shows the same comparison on CIFAR at $k = 154$ using the deep AIQT with depth $D = 4$. With the same coefficient budget, the deep AIQT better preserves object contours (e.g., vehicle edges and bird outlines), local textures (such as fur and feathers), and smooth color transitions, whereas the Fourier reconstructions appear washed out and lose fine detail.

Table 3 reports the performance of the deep AIQT on MNIST and CIFAR at fixed sparsity ($k = 52$ for MNIST, $k = 154$ for CIFAR), comparing different depths D to the FSL baseline. On all three datasets, increasing depth from $D = 1$ to $D = 4$ progressively

reduces cRMSE and increases fidelity on both training and validation splits. For MNIST, the deepest model ($D = 4$) nearly halves the validation cRMSE relative to the FSL (6.934×10^{-3} vs. 12.46×10^{-3}) and raises the fidelity from 0.8486 to 0.9515. On CIFAR-B&W and CIFAR-RGB, $D = 4$ likewise improves over the FSL, reducing validation cRMSE by about 17% and 16%, respectively, while increasing fidelity.

Discussion

We applied the adaptive interpolating quantum transform (AIQT) as a replacement for the Fourier transform in sparse amplitude encoding of real-world data. By learning a data-adaptive basis, the AIQT reduces the information lost in the coefficient truncation step, maximizing the information captured by the retained coefficients. On a one-dimensional finance dataset, the AIQT cut validation reconstruction error by about 40% relative to the Fourier-based method at matched sparsity, while also improving fidelity. More importantly, for this dataset the AIQT scales more favorably with the sparsity budget: as k increases, the approximation cRMSE decays more rapidly than for the FSL. Although the AIQT does not inherit the exact real-valued guarantee of the Fourier transform, our experiments show that the trained models naturally suppress imaginary leakage: the imaginary-part norm drops by several orders of magnitude during training, and the reconstructed states remain almost perfectly real-valued across sparsity levels. We also introduced a deep variant formed by stacking multiple AIQT blocks. This "deep AIQT" architecture further improves reconstruction quality on image data, achieving up to roughly 50% reduction in error and higher fidelity compared to the Fourier-based method. These results suggest that the AIQT provides a practical, quantum-native way to improve approximate amplitude encoding by reducing reconstruction error and improving fidelity at fixed sparsity. Moreover, for the shallow AIQT, these improvements are achieved at a similar gate cost to the FSL. Future work could incorporate gate-aware regularization into the loss function to further reduce encoding cost.

Thus, our work provides a data-driven approach to addressing a central practical bottleneck in quantum computing: quantum state preparation from classical data. In particular, the parameters of the AIQT can be trained from unlabeled inputs entirely on a classical computer, avoiding quantum-hardware sampling during training. Moreover, the FFT-like butterfly structure

of the AIQT yields a quasilinear classical forward cost in N (i.e., $O(N \log N)$), making training far cheaper than learning a generic dense $N \times N$ transform. The parameter count is also dramatically reduced: whereas an unconstrained $N \times N$ unitary scales with $O(N^2)$ parameters, the AIQT uses only $O(n^2)$ trainable parameters for $N = 2^n$. Once trained, the learned transform maps directly to a QFT-like quantum circuit with $O(n^2)$ gates on an n -qubit system. More broadly, the deep AIQT architecture increases expressivity and motivates exploring applications beyond sparse amplitude encoding.

Methods

The AIQT implementation, initialization, and training

We now describe the AIQT implementation used throughout this work. The AIQT is a trainable unitary transform with an FFT/QFT-like butterfly structure^{1,37,38}. For $N = 2^n$, the computation proceeds in n stages. At each stage, the vector is split into even and odd subsequences; the odd branch receives a trainable phase modulation that corresponds to controlled-phase operations in the AIQT circuit. The two branches are then mixed by a trainable 2×2 unitary parameterized as $U3(\alpha, \beta, \gamma)$ (Fig. 1c). The trainable parameters are the per-stage mixer angles (α, β, γ) and the controlled-phase angles $\theta \in \mathbb{R}^{n(n-1)/2}$.

We initialize the AIQT parameters to reproduce the quantum Fourier transform. Specifically, we set all mixer gates to $U3(\frac{\pi}{2}, 0, \pi)$ and initialize the controlled-phase gates as $CR(\theta) = \text{diag}(1, 1, 1, e^{i\theta})$ with phase angles

$$\theta_{\text{init}}^{(L)} = \left(-\frac{\pi}{2^L}, -\frac{\pi}{2^{L-1}}, \dots, -\frac{\pi}{2}\right), \quad L = 1, \dots, n-1, \quad (12)$$

which we pack as

$$\theta_{\text{Fourier}} = (\theta_{\text{init}}^{(1)}, \dots, \theta_{\text{init}}^{(n-1)}). \quad (13)$$

Here, L indexes the phase-ladder levels, of which there are $n - 1$ for an n -qubit system.

To minimize $\mathcal{L}_{\text{tail}}$ using automatic differentiation, we address the non-differentiable nature of the discrete coefficient selection $\mathcal{K}(x)$. We therefore optimize a differentiable relaxation of the loss using a sigmoid-based soft mask (temperature $\tau = 10^{-2}$)

Table 3 Performance of the deep AIQT on MNIST and CIFAR. The deep AIQT results are reported for circuit depths $D \in \{1, 2, 4\}$. For sparsification, we use $k = 52$ for MNIST and $k = 154$ for CIFAR.

Dataset	k	D	Training		Validation	
			cRMSE $\times 10^{-3}$	F	cRMSE $\times 10^{-3}$	F
MNIST	52	1	12.56	0.8462	12.53	0.8469
		2	8.623	0.9255	8.588	0.9261
		4	6.957	0.9512	6.934	0.9515
		FSL	—	—	12.46	0.8486
CIFAR-B&W	154	1	3.476	0.9877	3.479	0.9877
		2	3.232	0.9893	3.228	0.9894
		4	2.867	0.9916	2.863	0.9916
		FSL	—	—	3.470	0.9877
CIFAR-RGB	154	1	3.575	0.9870	3.576	0.9870
		2	3.303	0.9889	3.299	0.9889
		4	3.034	0.9906	3.031	0.9906
		FSL	—	—	3.590	0.9870

computed from coefficient energies relative to the k -th largest threshold, with gradients propagated via a straight-through estimator. To improve convergence stability and discourage degenerate uniform-energy solutions, we add a small entropy regularization term ($\lambda = 10^{-4}$) to the objective function.

We optimize the parameters of the AIQT using Adam for 150 epochs (batch size 128) and a cosine-annealing learning-rate schedule that decays over the first two-thirds of training and is held at its minimum value for the final third.

Coefficient selection

As described in the workflow in Section [Transform-based Approximate Amplitude Encoding](#), given coefficients $\mathbf{y}(\mathbf{x})$, we form an index set $\mathcal{K}(\mathbf{x})$ that specifies which coefficients are retained in the top- k truncation step. In this subsection, we describe how $\mathcal{K}(\mathbf{x})$ is constructed for the AIQT and FSL workflows.

For coefficient selection in the AIQT workflow, we construct $\mathcal{K}(\mathbf{x})$ by selecting the indices of the k largest coefficients of $\mathbf{y}(\mathbf{x})$ in squared magnitude. For the FSL baseline, coefficient selection must preserve the conjugate symmetry that arises in Fourier coefficients of real-valued inputs. Accordingly, our truncation step explicitly enforces conjugate symmetry when constructing $\mathcal{K}(\mathbf{x})$ as follows. We first include the first coefficient $j = 1$ and, for even N , the middle coefficient $j = N/2 + 1$ in $\mathcal{K}(\mathbf{x})$. These are always retained

and do not count against the top- k budget. We then form conjugate-symmetric pairs $(j, N + 2 - j)$ for $j = 2, \dots, N/2$ and rank these pairs by $m_j(\mathbf{x}) + m_{N+2-j}(\mathbf{x})$, with $m_j(\mathbf{x})$ defined in Eq. 5. From this ordering, we select the top $k/2$ pairs and include both indices j and $N + 2 - j$ from each selected pair in $\mathcal{K}(\mathbf{x})$. Thus, a top- k budget corresponds to k coefficients drawn from conjugate-symmetric pairs and, together with the first and middle coefficients, yields $|\mathcal{K}(\mathbf{x})| = k + 2$.

Datasets

Motivated by future applications in quantum finance and quantum image processing, we evaluate the performance of our method and the FSL on three datasets: a 1-D financial time-series dataset and two 2-D image datasets (MNIST and CIFAR). The financial dataset comprises stock prices sampled every 2 minutes for 217 companies, sourced from Yahoo Finance³⁹. Each series is segmented into overlapping windows of length $N = 1024$ with a stride of 128 points, yielding 8669 samples in total. We split these chronologically into 80% training and 20% validation. For MNIST and CIFAR, we use 50k images from each dataset, considering both CIFAR-RGB (color) and CIFAR-B&W (grayscale), and apply an 80/20 training/validation split. Each image is resized to 32×32 , resulting in an input dimension $N = 1024$.

Evaluation metrics

To compare the performance of the AIQT and the FSL, we use two metrics: the complex root-mean-squared error (cRMSE) and the fidelity (F). For each input \mathbf{x} , let $|\psi(\mathbf{x})\rangle$ denote the exact amplitude-encoded quantum state and $|\tilde{\psi}(\mathbf{x})\rangle$ the reconstructed quantum state. Writing their amplitude vectors as $\psi(\mathbf{x}), \tilde{\psi}(\mathbf{x}) \in \mathbb{C}^N$ with components $\psi_j(\mathbf{x})$ and $\tilde{\psi}_j(\mathbf{x})$, we define the error components $e_j(\mathbf{x}) = \tilde{\psi}_j(\mathbf{x}) - \psi_j(\mathbf{x})$. The complex RMSE between $|\psi(\mathbf{x})\rangle$ and $|\tilde{\psi}(\mathbf{x})\rangle$ is then

$$\text{cRMSE}(|\psi(\mathbf{x})\rangle, |\tilde{\psi}(\mathbf{x})\rangle) = \left(\frac{1}{N} \sum_{j=1}^N |e_j(\mathbf{x})|^2 \right)^{1/2}. \quad (14)$$

The fidelity between $|\psi(\mathbf{x})\rangle$ and $|\tilde{\psi}(\mathbf{x})\rangle$ is defined as

$$F(|\psi(\mathbf{x})\rangle, |\tilde{\psi}(\mathbf{x})\rangle) = |\langle \psi(\mathbf{x}) | \tilde{\psi}(\mathbf{x}) \rangle|^2, \quad (15)$$

where $\langle \psi(\mathbf{x}) | \tilde{\psi}(\mathbf{x}) \rangle$ denotes the standard complex inner product. We report cRMSE and F averaged over all samples in the dataset.

The entire workflow was implemented using the PyTorch framework.

Acknowledgements. This work was supported by JSPS KAKENHI under Grant-in-Aid for Early-Career Scientists No. JP24K16985 and JSPS KAKENHI under Grant-in-Aid for Transformative Research Areas No. JP22H05114. This study was partially carried out using the facilities of the Supercomputer Center, the Institute for Solid State Physics, the University of Tokyo (ISSPkyodo-SC-2025-Eb-0008, 2025-Ea-0013) and the TSUBAME4.0 supercomputer at the Institute of Science Tokyo. This work was partially supported by the Center of Innovations for Sustainable Quantum AI (JST Grant Number JPMJPF2221). This work was supported by Japan Science and Technology Agency (JST) as part of Adopting Sustainable Partnerships for Innovative Research Ecosystem (ASPIRE), Grant Number JPMJAP24C1. The author acknowledges the contributions and discussions provided by the members of Quemix Inc.

References

- [1] Nielsen, M. A. & Chuang, I. L. *Quantum Computation and Quantum Information: 10th Anniversary Edition* (Cambridge University Press, Cambridge, UK, 2010).
- [2] Kjaergaard, M. *et al.* Superconducting qubits: Current state of play. *Annual Review of Condensed Matter Physics* **11**, 369–395 (2020). URL <https://www.annualreviews.org/content/journals/10.1146/annurev>
- [3] McArdle, S., Endo, S., Aspuru-Guzik, A., Benjamin, S. C. & Yuan, X. Quantum computational chemistry. *Rev. Mod. Phys.* **92**, 015003 (2020). URL <https://link.aps.org/doi/10.1103/RevModPhys.92.015003>.
- [4] Endo, S., Cai, Z., Benjamin, S. C. & Yuan, X. Hybrid quantum-classical algorithms and quantum error mitigation. *Journal of the Physical Society of Japan* **90**, 032001 (2021). URL <https://doi.org/10.7566/JPSJ.90.032001>.
- [5] Cerezo, M. *et al.* Variational quantum algorithms. *Nature Reviews Physics* **3**, 625–644 (2021). URL <http://dx.doi.org/10.1038/s42254-021-00348-9>.
- [6] Bharti, K. *et al.* Noisy intermediate-scale quantum algorithms. *Rev. Mod. Phys.* **94**, 015004 (2022). URL <https://link.aps.org/doi/10.1103/RevModPhys.94.015004>.
- [7] Xiao, T., Fan, J. & Zeng, G. Parameter estimation in quantum sensing based on deep reinforcement learning. *npj Quantum Information* **8** (2022). URL <http://dx.doi.org/10.1038/s41534-021-00513-z>.
- [8] Xiao, T., Zhai, X., Wu, X., Fan, J. & Zeng, G. Practical advantage of quantum machine learning in ghost imaging. *Communications Physics* **6** (2023). URL <http://dx.doi.org/10.1038/s42005-023-01290-1>.
- [9] Budiutama, G. *et al.* Channel attention for quantum convolutional neural networks. *Phys. Rev. A* **110**, 012447 (2024). URL <https://link.aps.org/doi/10.1103/PhysRevA.110.012447>.
- [10] Grover, L. K. Synthesis of quantum superpositions by quantum computation. *Phys. Rev. Lett.* **85**, 1334–1337 (2000). URL <https://link.aps.org/doi/10.1103/PhysRevLett.85.1334>.

- [11] Long, G.-L. & Sun, Y. Efficient scheme for initializing a quantum register with an arbitrary superposed state. *Phys. Rev. A* **64**, 014303 (2001). URL <https://link.aps.org/doi/10.1103/PhysRevA.64.014303>.
- [12] Shende, V. & Markov, I. Quantum circuits for incompletely specified two-qubit operators. *Quantum Information and Computation* **5**, 48–56 (2005). URL <http://dx.doi.org/10.26421/QIC5.1-5>.
- [13] Möttönen, M., Vartiainen, J. J., Bergholm, V. & Salomaa, M. M. Transformation of quantum states using uniformly controlled rotations. *Quantum Info. Comput.* **5**, 467–473 (2005).
- [14] Plesch, M. & Brukner, i. c. v. Quantum-state preparation with universal gate decompositions. *Phys. Rev. A* **83**, 032302 (2011). URL <https://link.aps.org/doi/10.1103/PhysRevA.83.032302>.
- [15] Zhang, X.-M., Yung, M.-H. & Yuan, X. Low-depth quantum state preparation. *Phys. Rev. Res.* **3**, 043200 (2021). URL <https://link.aps.org/doi/10.1103/PhysRevResearch.3.043200>.
- [16] Soklakov, A. N. & Schack, R. Efficient state preparation for a register of quantum bits. *Phys. Rev. A* **73**, 012307 (2006). URL <https://link.aps.org/doi/10.1103/PhysRevA.73.012307>.
- [17] Wang, H., Ashhab, S. & Nori, F. Efficient quantum algorithm for preparing molecular-system-like states on a quantum computer. *Phys. Rev. A* **79**, 042335 (2009). URL <https://link.aps.org/doi/10.1103/PhysRevA.79.042335>.
- [18] Park, D. K., Petruccione, F. & Rhee, J.-K. K. Circuit-based quantum random access memory for classical data. *Scientific Reports* **9** (2019). URL <http://dx.doi.org/10.1038/s41598-019-40439-3>.
- [19] Ashhab, S. Quantum state preparation protocol for encoding classical data into the amplitudes of a quantum information processing register’s wave function. *Phys. Rev. Res.* **4**, 013091 (2022). URL <https://link.aps.org/doi/10.1103/PhysRevResearch.4.013091>.
- [20] Kosugi, T., Daimon, S., Nishi, H., Tsuneyuki, S. & Matsushita, Y.-i. Qubit encoding for a mixture of localized functions. *Phys. Rev. A* **110**, 062407 (2024). URL <https://link.aps.org/doi/10.1103/PhysRevA.110.062407>.
- [21] Zoufal, C., Lucchi, A. & Woerner, S. Quantum generative adversarial networks for learning and loading random distributions. *npj Quantum Information* **5** (2019). URL <http://dx.doi.org/10.1038/s41534-019-0223-2>.
- [22] Nakaji, K. *et al.* Approximate amplitude encoding in shallow parameterized quantum circuits and its application to financial market indicators. *Phys. Rev. Res.* **4**, 023136 (2022). URL <https://link.aps.org/doi/10.1103/PhysRevResearch.4.023136>.
- [23] Daimon, S. & Matsushita, Y.-i. Quantum circuit generation for amplitude encoding using a transformer decoder. *Phys. Rev. Appl.* **22**, L041001 (2024). URL <https://link.aps.org/doi/10.1103/PhysRevApplied.22.L041001>.
- [24] Mitsuda, N. *et al.* Approximate complex amplitude encoding algorithm and its application to data classification problems. *Phys. Rev. A* **109**, 052423 (2024). URL <https://link.aps.org/doi/10.1103/PhysRevA.109.052423>.
- [25] Moosa, M., Watts, T. W., Chen, Y., Sarma, A. & McMahon, P. L. Linear-depth quantum circuits for loading fourier approximations of arbitrary functions. *Quantum Science and Technology* **9**, 015002 (2023). URL <https://doi.org/10.1088/2058-9565/acfc62>.
- [26] Ko, T., Lee, I. & Yu, H. W. Quantum medical image encoding and compression using fourier-based methods (2025). URL <https://arxiv.org/abs/2505.06471>. arXiv:2505.06471.
- [27] Boosari, E. R. F. & Afsary, M. Hybrid quantum state preparation via data compression (2025). URL <https://arxiv.org/abs/2512.01798>. arXiv:2512.01798.
- [28] Budiutama, G., Daimon, S., Nishi, H. & Ichiro Matsushita, Y. General transform: A unified framework for adaptive transform to enhance representations (2025).

- URL <https://arxiv.org/abs/2505.04969>.
arXiv:2505.04969.
- [29] Budiutama, G. *et al.* Adaptive interpolating quantum transform: A quantum-native framework for efficient transform learning. *Phys. Rev. A* **112**, 062410 (2025). URL <https://link.aps.org/doi/10.1103/vyr3-h9hq>.
- [30] Malvetti, E., Iten, R. & Colbeck, R. Quantum Circuits for Sparse Isometries. *Quantum* **5**, 412 (2021). URL <https://doi.org/10.22331/q-2021-03-15-412>.
- [31] Zhang, X.-M., Li, T. & Yuan, X. Quantum state preparation with optimal circuit depth: Implementations and applications. *Phys. Rev. Lett.* **129**, 230504 (2022). URL <https://link.aps.org/doi/10.1103/PhysRevLett.129.230504>.
- [32] de Veras, T. M. L., da Silva, L. D. & da Silva, A. J. Double sparse quantum state preparation. *Quantum Information Processing* **21** (2022). URL <http://dx.doi.org/10.1007/s11128-022-03549-y>.
- [33] Mozafari, F., De Micheli, G. & Yang, Y. Efficient deterministic preparation of quantum states using decision diagrams. *Phys. Rev. A* **106**, 022617 (2022). URL <https://link.aps.org/doi/10.1103/PhysRevA.106.022617>.
- [34] Ramacciotti, D., Lefterovici, A. I. & Rotundo, A. F. Simple quantum algorithm to efficiently prepare sparse states. *Phys. Rev. A* **110**, 032609 (2024). URL <https://link.aps.org/doi/10.1103/PhysRevA.110.032609>.
- [35] Mao, R., Tian, G. & Sun, X. Toward optimal circuit size for sparse quantum state preparation. *Phys. Rev. A* **110**, 032439 (2024). URL <https://link.aps.org/doi/10.1103/PhysRevA.110.032439>.
- [36] Li, L. & Luo, J. Censor-Hillel, K., Grandoni, F., Ouaknine, J. & Puppis, G. (eds) *Nearly Optimal Circuit Size for Sparse Quantum State Preparation*. (eds Censor-Hillel, K., Grandoni, F., Ouaknine, J. & Puppis, G.) *52nd International Colloquium on Automata, Languages, and Programming (ICALP 2025)*, Vol. 334 of *Leibniz International Proceedings in Informatics (LIPIcs)*, 113:1–113:19 (Schloss Dagstuhl – Leibniz-Zentrum für Informatik, Dagstuhl, Germany, 2025). URL <https://drops.dagstuhl.de/entities/document/10.4230/LIPIcs.ICALP.2025.113:1-113:19>.
- [37] Cooley, J. W. & Tukey, J. W. An algorithm for the machine calculation of complex fourier series. *Mathematics of Computation* **19**, 297–301 (1965). URL <http://www.jstor.org/stable/2003354>.
- [38] Dao, T., Gu, A., Eichhorn, M., Rudra, A. & Ré, C. Chaudhuri, K. & Salakhutdinov, R. (eds) *Learning fast algorithms for linear transforms using butterfly factorizations*. (eds Chaudhuri, K. & Salakhutdinov, R.) *Proceedings of the 36th International Conference on Machine Learning*, Vol. 97 of *PMLR*, 1517–1527 (2019).
- [39] Yahoo finance: Historical market data. <https://finance.yahoo.com/>.